Automated 3D Reconstruction and Segmentation from Optical Coherence Tomography

Justin A. Eichel[1], Kostadinka K. Bizheva[2], David A. Clausi[1], and Paul W. Fieguth[1]

[1] Systems Design Engineering, University of Waterloo, Canada
[2] Department of Physics and Astronomy, University of Waterloo, Canada
{jaeichel,kbizheva,dclausi,pfieguth}@uwaterloo.ca

Abstract. Ultra-High Resolution Optical Coherence Tomography is a novel imaging technology that allows non-invasive, high speed, cellular resolution imaging of anatomical structures in the human eye, including the retina and the cornea.

A three-dimensional study of the cornea, for example, requires the segmentation and mutual alignment of a large number of two-dimensional images. Such segmentation has, until now, only been undertaken by hand for individual two-dimensional images; this paper presents a method for automated segmentation, opening substantial opportunities for 3D corneal imaging and analysis, using many hundreds of 2D slices.

Keywords: OCT, UHROCT, cornea, non-invasive imaging, statistical modelling, segmentation, reconstruction.

1 Introduction

Optical Coherence Tomography is an optical imaging technique that allows for non-invasive (non-contact), micrometer-scale imaging of transparent objects and biological tissue. Some of the most advanced medical applications of OCT are in the field of ophthalmology for non-invasive imaging of healthy and diseased human retina and cornea [1–4].

The human cornea, which is the application focus of our research, consists of five distinct layers of variable thickness: Epithelium ($\sim 50\mu m$), Bowman's membrane ($\sim 15\mu m$), Stroma ($\sim 500\mu m$), Descemet's membrane ($\sim 10\mu m$) and Endothelium ($\sim 5\mu m$), labeled in Figure 1. Identifying individual corneal layers in OCT tomograms and the precise measurement of their thicknesses is essential in the evaluation of corneal disease, for example to study the progression and treatment of Keratitis, Keratoconus, Fuchs' dystrophy, and Hypoxia [5–8], as these corneal diseases transform the shape and layer thickness of the cornea.

Until now, corneal layer segmentation has only been undertaken by hand for individual 2D images, greatly limiting the types of problems or number of patients who could be studied, and making completely impractical any 3D study based on the segmentation and registration of hundreds of 2D images.

K. Daniilidis, P. Maragos, N. Paragios (Eds.): ECCV 2010, Part III, LNCS 6313, pp. 44–57, 2010.

This paper presents a method for automated segmentation, opening substantial opportunities for 3D corneal imaging and analysis. The proposed segmentation method is the first fully automated algorithm, to the author's knowledge, that can segment the five corneal layers based on Optical Coherence Tomography images. Since both boundaries of the Descemet's membrane are less than the imaging resolution, the Descemet's Endothelium complex is represented by a single boundary instead. The data in this paper were acquired with an UltraHigh Resolution Optical Coherence Tomography (UHROCT) system, which allows for non-invasive imaging of a human cornea with $3\mu m$ axial resolution and an acquisition rate of 47,000 2D scans per second [9].

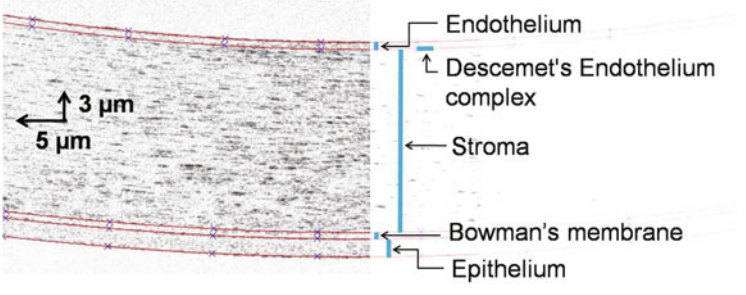

Fig. 1. UHROCT image of the cornea containing labeled layer boundaries

The Background section discusses existing 3D corneal reconstruction techniques and segmentation algorithms. The Reconstruction Method section describes the novel 2D segmentation algorithm, developed in this paper, applied to multiple cornea images, leading to the development of an approach for 3D reconstruction.

2 Background

The proposed method intends to extend existing reconstruction techniques so that a 3D model can be obtained from a series of noisy UHROCT images. The following sections describe existing reconstruction methods and several segmentation methods that can be used to facilitate corneal reconstruction.

2.1 3D Reconstruction

Existing medical imaging techniques can be utilized for imaging large organs, such as the brain using MRI, or imaging small cells using electron microscopy. Depending on the scale of the object, different reconstruction algorithms are applied to the data collected from the imaging process.

When performing gross medical imaging, a series of 2D images might be stacked together if the object motion and the imaging system motion is

negligible compared to the overall dimensions of the object. For example, when performing ultra-sound to image large organs, the vibrations of the ultra-sound probe and the small motion of muscles surrounding the organs are insignificant due to the relative scale of the object being imaged [10]. In addition, stacking can be acceptable if a stationary object reference is visible in each frame. When performing a brain MRI, the stationary bone structure of the skull can be used to translate the 2D scans for the registration process [11].

Although on the smaller scale, electron microscopy is used to image cells. In these cases, the vibrations and motions of the cells are significant. However, like in gross medical imaging, electron microscopy can use reference points that are present in multiple 2D images [12]. Single-particle analysis [13, 14] attempts to identify macromolecules in each view and attempts to determine the orientation of each macromolecule in the particle.

Scarpa presents a method to reconstruct a cornea from confocal microscope imaging [15]. A region of interest is identified in each sequential set of images, then a normalized correlation method [16] is applied to the region of interest to find correspondences between the image frames. The images in the stack are translated to align the correspondences in consecutive images. The process, however, does not directly utilize the corneal layer boundaries for reference. The process also relies on a stack of images instead of using images perpendicular to the stack to assist with alignment.

Li applied confocal microscopy through focusing to measure the central layer thickness of the Epithelium, Bowman's layer, and total corneal thickness [17]. Although the approach is limited to manually measuring the central thickness, it was the first technique to obtain measurements for three of the five corneal layers. The proposed algorithm automates the manual process and extends the segmentation to all five corneal layer boundaries.

Currently, corneal OCT images may be aligned using a software package from Amira. Amira provides a suit of tools that can be used to align a stack of OCT images by comparing the direct image intensity and any salient features contained in sequential images [18, 19]. The software also allows the users to manually align the images. Unfortunately, the package does not use the structural properties of the cornea in the reconstruction process, preventing a suitable 3D reconstruction, and the 3D reconstructions generated failed to yield the accuracy necessary for corneal layer thickness research.

The proposed method attempts to automate and extend the 3D reconstruction process by utilizing the corneal layer boundaries and orthogonal UHROCT images to establish accurate point correspondences.

2.2 Segmentation

The proposed 3D reconstruction algorithm requires the segmentation of the corneal layer boundaries within the 2D UHROCT images.

Snakes and active contours are curves designed to surround lines and shapes that may be present in the image [20–24]. The active contour converges when the sum of internal (prior) and external (measurement) forces are minimized, such

that the internal forces prefer contour smoothness (or some other prior shape), and the external forces prefer a fit to the given image, normally related to the image gradient.

The concept of intelligent scissors [25] allows the user to semi-manually segment the image. By placing points on the image, the user guides the intelligent scissor algorithm, which snaps to the image gradient as the algorithm fits a curve through the user-defined points. The advantage of this algorithm is that the user can specify a few points on each corneal layer boundary while the algorithm fits a curve to the image gradient that follows the layer boundaries. When applied to a smooth image gradient, the algorithm can fit a curve to the gradient with little user interaction. However, when applied to the UHROCT images, the intelligent scissors fit the noise obscured the otherwise smooth gradient preventing the effective segmentation of the boundaries. Figure 2(b) illustrates the performance of the algorithm despite having the user generate 20 to 30 points for each layer.

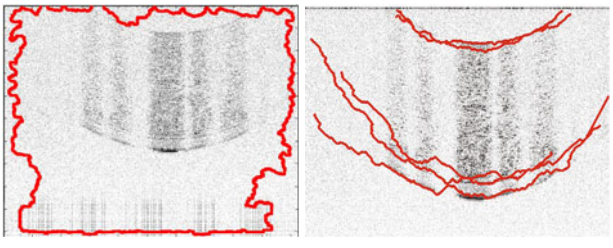

Fig. 2. UHROCT segmentation results for (left) geometric active contour and (right) intelligent scissors. Neither method produces accurate segmentation results.

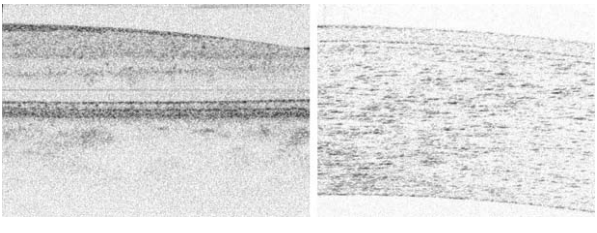

Fig. 3. Comparison of retinal (left) and corneal (right) UHROCTs. Unlike corneal layers, each retinal layer has a visibly distinct intensity compared to adjacent layers. In contrast, corneal layers contain a visible thin, dark boundary between each layer.

While many well developed retinal OCT imaging techniques exist to identify layer boundaries of the retina, corneal imaging provides different challenges.

Garvin proposes the use of a general graph-based approached that attempts to reconstruct the retinal images into a 3D model and isolate the surfaces that correspond to the retinal layers [26]. In addition, Mishra developed a method using image gradient information and a kernel function to successfully compensate for the speckle noise, present in OCT images, and efficiently segments retinal layers [27]. The major difference between retinal and corneal segmentation is due to composition of the layers. As shown in Figure 3, unlike the cornea, the retinal layers have different mean intensities for each layer. The retinal methods are good at finding the edge between these layers. In contrast, corneal layers have a similar mean intensity, but are separated by low-contrast, discontinuous, thin layer boundaries instead. As a result, retinal methods were able to find the high contrast outer layers, but could not locate the inner layers.

3 Reconstruction Method

A variety of active contours, including parametric, geometric, and edge-free, were implemented and tested on UHROCT images. Not one of the implemented methods was able to segment the cornea; Figure 2(a) illustrates a typical example of the final state of a geometric active contour [28]. In many ways this failure is unsurprising: the images are noisy, the contours have frequent breaks, and the active-contour methods have only a weak prior (smoothness) which knows very little about corneal structure.

The failure of existing algorithms to segment the corneal layer boundaries motivated the development of a method to perform 2D corneal segmentation. The proposed method imposes a corneal model on the data to allow the corneal layer boundaries to be segmented, despite the presence of noise and imaging artefacts.

The reconstruction process consists of two major steps. The 2D UHROCT images are first segmented so that each of the five layer boundaries can be obtained and the layers are subsequently used as markers to for a second step, the 3D reconstruction. These two respective steps are described in the following two sections.

3.1 2D Reconstruction

The 2D reconstruction uses a corneal model to locate the internal layers of the cornea. The starting point is to observe that the upper and lower corneal layers have sufficient contrast, due to the high refractive index at the interface between the cornea and the surrounding fluid, to segment these layers robustly. The model then asserts that all internal layers can be derived using the curvature information from the upper and lower corneal layers.

Let the data acquired from the UHROCT imaging device be a 2D greyscale image $I(x, y)$. During the imaging process, a higher contrast endothelium layer can be obtained by focusing the UHROCT system on the endothelium layer instead of the epithelium layer. Since the epithelium layer boundary is the interface

between air and the cornea, the refractive index can produce sufficient contrast for the segmentation algorithm. The focusing emphasizes the contrast of the endothelium layer. However, as a consequence the cornea becomes inverted on the image plane, as seen in Figure 4(a).

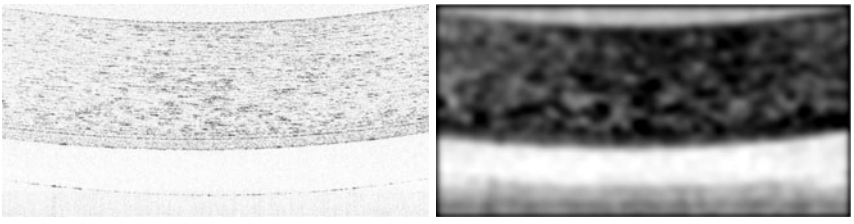

(a) (b)

Fig. 4. (a) The original UHROCT image obtained from the imaging system. (b) The result of preprocessing applied to the original UHROCT image, to improve contrast to robustly find the upper and lower layers.

The UHROCT layer boundaries appear quite noisy. The boundaries are about one to two pixels thick, have a varying pixel intensity, and are surrounded by what appears to be speckle or correlated noise, actually due to the distribution of cells within the cornea. To improve segmentation accuracy in the presence of noise, image preprocessing is undertaken by applying contrast-limited adaptive histogram equalization [29] to normalize pixel intensities across the image, morphological operators to enhance arc structures, and a Gaussian blur filter to smooth the remaining noise. The resulting preprocessed image, $I_{pre}(x, y)$, shown in Figure 4(b), contains sufficient contrast to clearly separate the cornea from the surrounding fluid.

As a most basic segmentation of cornea from fluid, a Prewitt edge detector is applied to find horizontal edges fragments in $I_{pre}(x, y)$, producing edge map $I_{edge}(x, y)$, containing edges that correspond to the upper and lower boundaries, as shown in Figure 5(a). Candidate endothelium / epithelium pixel locations are determined by locating those edges stronger than some threshold in the upper / lower half of I_{edge}.

Manually-segmented boundaries were available for a limited number of images, making it possible to learn a model and as ground truth in assessing the learned layers. Then an optimization problem is formulated to fit a quadratic curve, $Q_{end}(s)$ over arc-length s, to the upper layer boundary. An initial quadratic polynomial, $Q_{end}(s)$, based on statistics from the manual boundaries, was used to specify an initial curve for the optimization algorithm, as shown in Figure 5(b), where

$$\sum_{\forall p \epsilon P_{end}} \left[\min_{s} \|p - Q_{end}(s)\|_2 \right] \tag{1}$$

is minimized, minimizing the Euclidean distance from the curve to all thresholded edge points.

The quadratic is robust, but not a terribly good fit to the anatomy of the cornea. Various polynomials were tested to find the lowest order that could best model the corneal curvature. Since the difference between 5th and 4th-order polynomials was insignificant a 4th-order polynomial was selected to model the data. Having found the optimal quadratic fit, outlier rejection was performed by point trimming and the best 4th-order polynomial fit $Q^*_{end}(s)$ was found. The preceding process was applied, unchanged, to the bottom half of the edge points to find the best-fit curve to the epithelium $Q^*_{epi}(s)$.

Both curves, $\Omega^*_{end}(s)$ and $\Omega^*_{epi}(s)$, are illustrated in Figure 5(c).

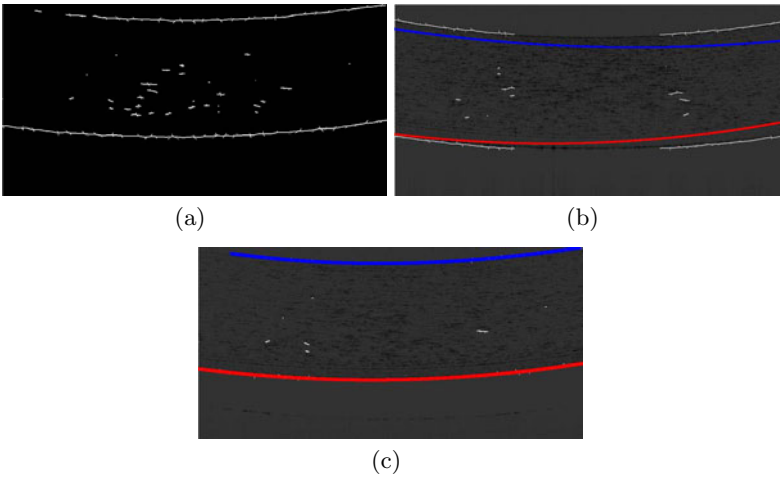

Fig. 5. (a) Edge detection applied to the preprocessed OCT Image. (b) The initial model of the upper and lower curves are independent of UHROCT image. (c) The segmentation of the upper and lower layer boundaries.

The model asserts that a continuous transformation exists that maps the Endothelium to the Epithelium; consequently, the curves representing the three internal layer boundaries are expressed as a low-dimensional parameterized function that uses the upper and lower curves as a basis:

$$\Omega^{\alpha=0}(s) = \Omega^0_{epi}(s - s_0) \qquad \Omega^{\alpha=1}(s) = \Omega^0_{end}(s - s_1) \tag{2}$$

The parameterized corneal model is illustrated in Figure 6. Any of the five corneal layers can be represented by the parameterized curve $\Omega^\alpha(s)$, where parameter α provides a mechanism to continuously transition between the upper and lower curves:

$$\Omega^\alpha(s) = (1 - \alpha)\Omega^{\alpha=0}(s) + \alpha\Omega^{\alpha=1}(s) \tag{3}$$

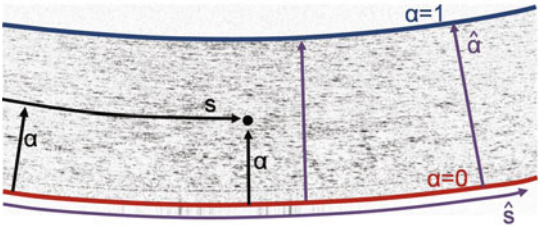

Fig. 6. Corneal model parametrization. s indexes along the arc, whereas α is essentially an interpolation parameter between the bottom ($\alpha = 0$) and top ($\alpha = 1$) curves.

where the parameters s_0 and s_1 are required to establish point correspondences between the upper and lower curves, established by the medial axis transform.

All five corneal layer boundaries are detected using a process essentially based on the generalized Hough transform [30]. The mean pixel intensity, μ_α of the UHROCT image, $I(x, y)$, is sampled along the curve $\Omega^\alpha(s)$ as a function of α:

$$\mu_\alpha = \frac{1}{n}\sum_{i=1}^{n} I\left(\Omega^\alpha\left(\frac{i}{n}\right)_x, \Omega^\alpha\left(\frac{i}{n}\right)_y\right) \tag{4}$$

An example of μ_α for a particular UHROCT is shown in Figure 7. The proposed algorithm applies a peak detector that identifies the peaks with the largest difference between the proximate maximum and minimum. In this example the five most significant peaks occur at $\alpha = [0.0930, 0.0138, 0.1227, 0.9917,$ and $0.9598]$, which correspond to the five corneal layers.

Figure 9 illustrates six examples of segmenting the five layers overlaid onto the original UHROCT image and illustrates the robustness of the algorithm when applied to UHROCT data containing imaging artifacts. It needs to be emphasized that the method is fully automated and that, to this point, no such algorithm has existed which is able to perform such a segmentation. The results are accurate, and robust in the presence of significant imaging artifacts.

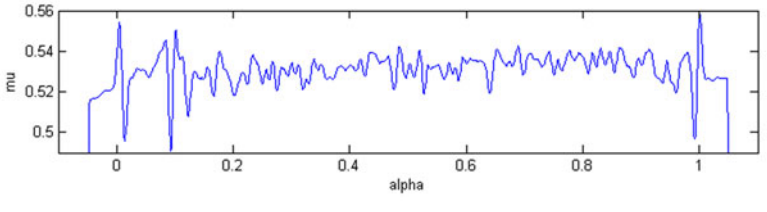

Fig. 7. A plot of the generalized Hough projection μ_α, projecting along corneal arcs, to identify prospective layers

3.2 3D Reconstruction

The novelty and performance of the 2D segmentation from the previous section is already a highly significant step in ophthalmologic research. Our ideal goal, however, is 3D reconstruction.

A 3D reconstruction of the cornea can be obtained from an ensemble of 2D segmented images either imaged in parallel or, preferably, in two orthogonal directions, as illustrated in Figure 8. Parallel imaging requires some sort of model regarding cross-plane behaviour, whereas perpendicular planes can be fused without prior assumptions, by using the intersections of the image planes as reference points for alignment. Since the primary source of alignment error is due to eye motion and camera vibration, it is reasonable to assume that the dominant inter-plane offsets are translational, rather than rotational or changes in scale. The local coordinates $\left|x\ y\ 0\ 1\right|_{\parallel}^{T}$, for the parallel images, and $\left|x\ y\ 0\ 1\right|_{\perp}^{T}$ for the perpendicular images are mapped to the global coordinates $\left|X\ Y\ Z\ 1\right|^{T}$ using the linear transformations

$$\begin{vmatrix} X \\ Y \\ Z \\ 1 \end{vmatrix} = H_{\parallel}^{0} \begin{vmatrix} x \\ y \\ 0 \\ 1 \end{vmatrix}_{\parallel} \quad \begin{vmatrix} X \\ Y \\ Z \\ 1 \end{vmatrix} = H_{\perp}^{0} \begin{vmatrix} x \\ y \\ 0 \\ 1 \end{vmatrix}_{\perp} \tag{5}$$

where

$$H_{\parallel}^{0} = \begin{vmatrix} 1 & 0 & 0 & x_o \\ 0 & 1 & 0 & y_o \\ 0 & 0 & 1 & z_o \\ 0 & 0 & 0 & 1 \end{vmatrix} \quad H_{\perp}^{0} = \begin{vmatrix} 0 & 0 & 1 & z_o \\ 0 & 1 & 0 & y_o \\ 1 & 0 & 0 & x_o \\ 0 & 0 & 0 & 1 \end{vmatrix} \tag{6}$$

The framework can be extended to six degrees of freedom by manipulating the homogeneous transformation matrices, where (5) transforms the local coordinates of $\Omega^{\alpha}(s)$ into global coordinates generating 3D coordinates for each layer boundary.

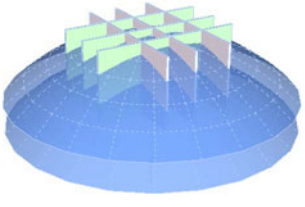

Fig. 8. Orientation of image planes for 3D Reconstruction, superimposed on the notional layers of a cornea

The intersection of the i^{th} parallel plane with the j^{th} perpendicular plane produces a line on both image planes. The intersection of this line with the layer

boundaries can produce point correspondences for each image. An optimization problem can be formulated to minimize the total Euclidean distance, in 3D space, between all of the corresponding points. The intersection of two lines can be derived by relating the coordinates the i^{th} parallel plane with the j^{th} perpendicular plane

$$\begin{vmatrix} x \\ y \\ 0 \\ 1 \end{vmatrix}_j = H_i^j \begin{vmatrix} x \\ y \\ 0 \\ 1 \end{vmatrix}_i = \begin{vmatrix} z_i - x_o^j \\ y_i + y_o^i - y_o^j \\ x_i + x_o^i - z_o^j \\ 1 \end{vmatrix} \tag{7}$$

using a homogeneous transformation, H_i^j,

$$H_i^j = \left(H_\perp^0\right)^{-1} H_\parallel^0 = H_0^\perp H_\parallel^0 = \begin{vmatrix} 0 & 0 & 1 & z_o^i - x_o^j \\ 0 & 1 & 0 & y_o^i - y_o^j \\ 1 & 0 & 0 & x_o^i - z_o^j \\ 0 & 0 & 0 & 1 \end{vmatrix} \tag{8}$$

The sequence of steps, below, in (9), defines the distance $d_{i,j}$ between the boundary layer defined by α_i on the i^{th} image plane and the corresponding boundary defined by α_j on the j^{th} image plane:

$$\begin{gathered} x_i = z_o^j - x_o^i \\ solve\left(\Omega_i^{\alpha_i}(s_i)_x = x_i, s_i\right) \\ y_i = \Omega_i^{\alpha_i}(s_i)_y \\ y_j = y_i + y_o^i - y_o^j \\ \\ x_j = z_o^i - x_o^j \\ solve\left(\Omega_j^{\alpha_j}(s_j)_x = x_j, s_j\right) \\ \\ d_{i,j}^2 = \left(y_j - \Omega_j^{\alpha_j}(s_j)_y\right)^2 \end{gathered} \tag{9}$$

The method is extensible to the general case, including rotations to allow six degrees of freedom, however the intersection line becomes significantly more complicated.

4 Results

The 2D segmentation algorithm has been tested on 2,050 UHROCT images obtained from 12 healthy subjects. The images were also manually segmented to provide ground truth. The proposed algorithm located the Epithelium and Endothelium boundaries to within about 2.5 pixels of the manually segmented images for all of the images, with a standard deviation of about 1.3 and 3.2 pixels, respectively. Table 1 contains the results in pixels and a approximation of μm for the other layers. These results can also be immediately improved by compensating for the segmentation bias. Each boundary is statistically too high in the image by between 0.7 to 3.7 pixels depending on the boundary. The boundaries can be systematically adjusted to reduce the error.

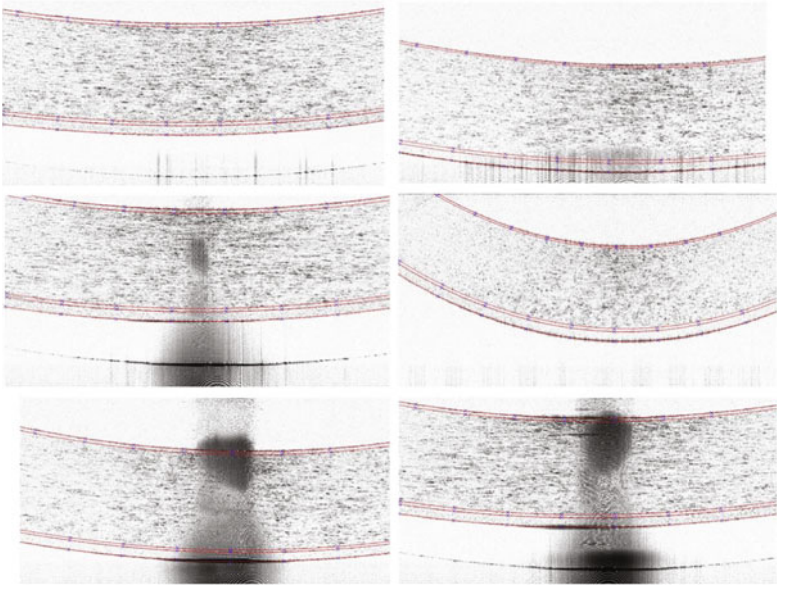

Fig. 9. Six examples of applying 2D corneal segmentation to OCT images. The model accomplishes exact segmentation, despite significant noise and varying corneal layer location within the image. The prominent imaging artifacts result from the high reflectively of the cornea when imaging near the apex.

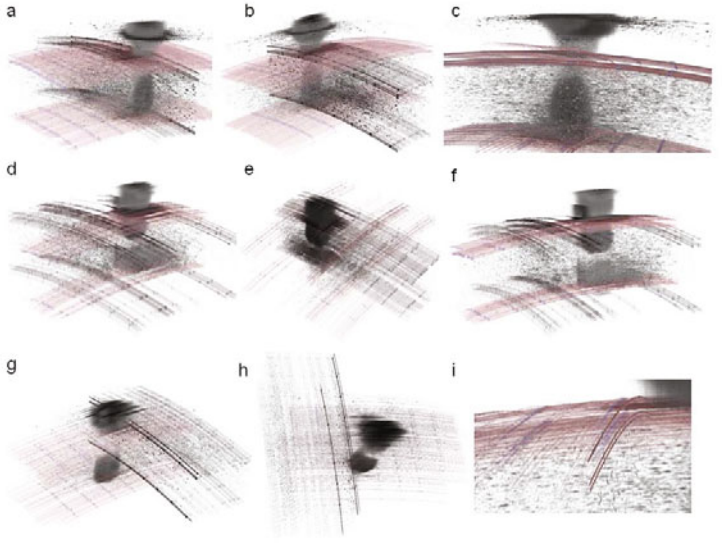

Fig. 10. Nine 3D Corneal reconstructions from the segmentation and mutual alignment of 2D UHROCT images. The images are taken from three subjects, one on each row. The segmentation results are superimposed on the underlying UHROCT data, which can be seen to have significant noise and artifacts.

Table 1. Segmentation Experimental Results

	Error			
Layer	Bias [pixels]	Std.Dev [pixels]	Bias [pixels] [μm]	Std.Dev [μm]
epi	1.32	1.26	3.92	4.38
bow	0.709	10.7	4.59	5.38
str	2.56	5.19	2.86	3.50
des	3.68	4.69	5.94	6.07
end	2.52	3.25	6.52	7.11

The 3D reconstruction algorithm used the results of the 2D segmentation algorithm applied to 3 healthy human subjects. Although four datasets were collected from each human subject, initial problems with the imaging procedure prevented the use of some data because the cornea moved out of the imaging plane as the subjects were being scanned. Figure 10 illustrates the 3D reconstruction obtained from the algorithm. Notice that the reconstruction for subject 2, image panes (d-f), contains sparse data due to the aforementioned imaging problem (since corrected). The figure visually shows how well the 3D reconstruction process aligned all of the layer boundaries, and supplementary material provided with this paper includes video, rotating the results in 3D to better illustrate how well the layers are aligned.

During the study, 442 UHROCT tomograms were successfully segmented for all three subjects. The segmentation process required approximately eight hours using MATLAB on a dual-core 2.5GHz laptop (if these layers were manually segmented, at an average rate of 15 minutes per image, it would take an experienced user about 110 hours). The advantage of the segmentation algorithm is that it is immune to fatigue and, given multiple processors, can segment UHROCT images in parallel. With such segmentation quality and reconstruction rates, the inference and clinical use of 3D corneal layer boundaries becomes quite feasible.

5 Conclusions

The method proposed in this paper is capable of automatically producing two-dimensional segmentations and three-dimensional reconstructions of a human cornea.

The proposed segmentation algorithm was applied to over two-thousand images, segmenting each *automatically*, a performance so far unmatched in any published method.

The three-dimensional corneal reconstruction is based on the simultaneous co-alignment of segmented two-dimensional frames, with each frame permitted translational degrees of freedom, to be optimized. The resulting three-dimensional reconstruction was successfully applied to three test subjects.

The ability to produce large, three-dimensional corneal reconstructions opens significant clinical and research opportunities. Collaborators in science and optometry are eager to continue refining the methodology, to allow future work in revealing details of corneal and retinal anatomy.

Further work can introduce additional degrees of freedom in the perpendicular planes to account for variance in planar orientation. Although perpendicular planes were proposed, there is no inherit requirement in the algorithm prohibiting planes of arbitrary orientation. Perpendicular planes were selected for imaging convenience.

Acknowledgment

The authors would like to thank C. Hyun, S. Hariri, N.Hutchings, T. Simpson assistance with the acquisition of the corneal images and helpful discussions. This research was sponsored by the Natural Sciences and Engineering Research Council (NSERC) of Canada as well as GEOIDE (GEOmatics for Informed Decisions). The 3D visualization was built using components from the Tech Soft 3D, LLC HOOPS 3D Library.

References

1. Povaay, B., Hermann, B., Unterhuber, A., Hofer, B., Sattmann, H., Zeiler, F., Morgan, J.E., Falkner-Radler, C., Glittenberg, C., Blinder, S., Drexler, W.: Three-dimensional optical coherence tomography at 1050 nm versus 800 nm in retinal pathologies: enhanced performance and choroidal penetration in cataract patients. J. Biomed. Opt. 12 (2007)
2. Akiba, M., Maeda, N., Yumikake, K., Soma, T., Nishida, K., Tano, Y., Chan, K.P.: Ultrahigh-resolution imaging of human donor cornea using full-field optical coherence tomography. J. Biomed. Opt. 12 (2007)
3. Jungwirth, J., Baumann, B., Pircher, M., Gtzinger, E., Hitzenberger, C.K.: Extended in vivo anterior eye-segment imaging with full-range complex spectral domain optical coherence tomography. J. Biomed. Opt. 14 (2009)
4. Gora, M., Karnowski, K., Szkulmowski, M., Kaluzny, B.J., Huber, R., Kowalczyk, A., Wojtkowski, M.: Ultra high-speed swept source imaging of the anterior segment of human eye at 200 khz with adjustable imaging range. Opt. Express. 17 (2009)
5. Martn-Navarro, C.M., Lorenzo-Morales, J., Cabrera-Serra, M.G., Rancel, F., Coronado-Alvarez, N., Piero, J., Valladares, B.: The potential pathogenicity of chlorhexidine-sensitive acanthamoeba strains isolated from contact lens cases from asymptomatic individuals in tenerife, canary islands, spain. J. Med. Microbiol. 57, 1399–1404 (2008); PMID: 18927419
6. Smolin, G., Foster, C.S., Azar, D.T., Dohlman, C.H.: Smolin and Thoft's The cornea. Lippincott Williams & Wilkins (2005)
7. Kostadinka, B., Hyun, C., Eichel, J., Hariri, S., Mishra, A., Clausi, D., Fieguth, P., Simpson, T., Hutchings, N., Manns, F., Soderberg, P.G., Ho, A.: Evaluation of hypoxic swelling of human cornea with high speed ultrahigh resolution optical coherence tomography. In: Ophthalmic Technologies XIX, San Jose, CA, USA, vol. 7163, pp. 71631G–71631G-6. SPIE (2009)
8. Snell, R.S., Lemp, M.A.: Clinical anatomy of the eye. Wiley-Blackwell (1998)
9. Drexler, W., Morgner, U., Ghanta, R.K., Kartner, F.X., Schuman, J.S., Fujimoto, J.G.: Ultrahigh-resolution ophthalmic optical coherence tomography. Nat. Med. 7, 502–507 (2001)

10. Colchester, A., Hawkes, D.J.: Information processing in medical imaging. Springer, Heidelberg (1991)
11. Hajnal, J.V., Hawkes, D.J., Hill, D.L.G.: Medical image registration. CRC Press, Boca Raton (2001)
12. Kuo, J.: Electron microscopy. Humana Press, Totowa (2007)
13. Frank, J.: Three-dimensional electron microscopy of macromolecular assemblies. Oxford University Press, US (2006)
14. Gu, J.: Structural bioinformatics, 2nd edn. Wiley-Blackwell, Hoboken (2009)
15. Scarpa, F.: In vivo three-dimensional reconstruction of the cornea from confocal microscopy images. In: Conf. Proc. IEEE Eng. Med. Biol. Soc., pp. 747–750 (2007)
16. Dani, P.: Automated assembling of images: image montage preparation. Pattern Recognition 28, 431 (1995)
17. Li, H.: Epithelial and corneal thickness measurements by in vivo confocal microscopy through focusing (CMTF). Current Eye Research 16, 214 (1997)
18. Reinhard, T., Larkin, D.F.P.: Cornea and external eye disease. Springer, Heidelberg (2006)
19. Stachs, O., Zhivov, A., Kraak, R., Stave, J., Guthoff, R.: In vivo three-dimensional confocal laser scanning microscopy of the epithelial nerve structure in the human cornea. Graefes Arch. Clin. Exp. Ophthalmol. 245, 569–575 (2007)
20. Kass, M., Witkin, A., Terzopoulos, D.: Snakes: Active contour models. Int. J. Comput. Vision 1, 321–331 (1988)
21. Amini, A.A., Weymouth, T.E., Jain, R.C.: Using dynamic programming for solving variational problems in vision. IEEE Transaction on Pattern Analysis and Machine Intelligence 12, 855–867 (1990)
22. Cohen, L.: On active contour models and balloons. Computer Vision Graphics and Image Understanding 53, 211–218 (1991)
23. Kass, M., Witkin, A., Terzopoulos, D.: Snakes: Active contour models. International Journal of Computer Vision 1, 321–331 (1988)
24. Malladi, R., Sethian, J.A., Vemuri, B.C.: Shape modeling with front propagation: A level set approach. IEEE Transaction on Pattern Analysis and Machine Intelligence 17, 158–175 (1995)
25. Mortensen, E.N., Barrett, W.A.: Intelligent scissors for image composition. In: Proc. 22nd Annu. Conf. on Comput. Graphics and Interact. Tech., vol. 22, pp. 191–198. ACM, New York (1995)
26. Garvin, M.K., Abrmoff, M.D., Wu, X., Russell, S.R., Burns, T.L., Sonka, M.: Automated 3-D intraretinal layer segmentation of macular spectral-domain optical coherence tomography images. IEEE Trans. Med. Imaging 28, 1436–1447 (2009); PMID: 19278927
27. Mishra, A., Wong, A., Bizheva, K., Clausi, D.A.: Intra-retinal layer segmentation in optical coherence tomography images. Opt. Express. 17, 23719–23728 (2009)
28. Caselles, V., Catt, F., Coll, T., Dibos, F.: A geometric model for active contours in image processing. Numerische Mathematik 66, 1–31 (1993)
29. Zuiderveld, K.: Contrast limited adaptive histogram equalization. In: Graphics Gems IV, pp. 474–485. Academic Press Professional, Inc., London (1994)
30. Ballard, D.H.: Generalizing the hough transform to detect arbitrary shapes. Pattern Recognition 13, 111–122 (1981)